

MATLAT: Material Latent Space for PBR Texture Generation

Kyeongmin Yeo Yunhong Min Jaihoon Kim Minhyuk Sung
KAIST



Figure 1. **PBR Textures Generated by MATLAT.** Our method produces PBR textures that accurately represent rough materials (left), metallic surfaces (middle), and complex mixed materials (right).

Abstract

We propose a generative framework for producing high-quality PBR textures on a given 3D mesh. As large-scale PBR texture datasets are scarce, our approach focuses on effectively leveraging the embedding space and diffusion priors of pretrained latent image generative models while learning a material latent space, MATLAT, through targeted fine-tuning. Unlike prior methods that freeze the embedding network and thus lead to distribution shifts when encoding additional PBR channels and hinder subsequent diffusion training, we fine-tune the pretrained VAE so that new material channels can be incorporated with minimal latent distribution deviation. We further show that correspondence-aware attention alone is insufficient for cross-view consistency unless the latent-to-image mapping preserves locality. To enforce this locality, we introduce a regularization in the VAE fine-tuning that crops latent patches, decodes them, and aligns the corresponding image regions to maintain strong pixel-latent spatial correspondence. Ablation studies and comparison with previous baselines demonstrate that our framework improves

PBR texture fidelity and that each component is critical for achieving state-of-the-art performance. Project page is at <https://matlat-proj.github.io>.

1. Introduction

Generative modeling has recently driven remarkable progress in 3D asset creation. Modern methods can synthesize geometry [6, 24, 36, 51], textures and materials [5, 26, 38, 50], motions and animations [16, 35, 44], and even complete assets and scenes [23, 28, 57]. Among these, a crucial requirement for production-ready assets is Physically Based Rendering (PBR) textures, which comprise albedo (diffuse color), roughness, and metallic channels. These channels enable physically accurate relighting under arbitrary illumination and are essential components of modern graphics pipelines.

Recent works on PBR texture generation [5, 7, 38, 46] advance beyond baked appearances by predicting material maps that enable relightable assets. However, progress remains constrained by the scarcity of large-scale, high-quality datasets with PBR channels, as the existing public dataset [8, 9] is limited to only tens of thousands of assets.

A natural direction to overcome this challenge is to leverage pretrained image generative models, which provide strong priors learned from large-scale RGB image datasets [39]. Techniques such as Score Distillation Sampling (SDS) [36] and its variants [31, 47] have been explored for this purpose, but they often fail to produce high-fidelity PBR material images and exhibit saturation artifacts. In practice, the most effective strategy has been to generate multi-view images with pretrained 2D models and then project them onto a mesh [7, 12, 17, 21, 26, 48, 50, 59, 60]. However, this multi-view generation approach still faces two major challenges for PBR texture synthesis. First, directly leveraging diffusion models trained on latent RGB images for PBR material generation is non-trivial, as PBR textures include additional channels (roughness and metallic). Simply mapping these channels to the pretrained encoder leads to a substantial domain gap. Second, preserving multi-view consistency is challenging, and its failure can lead to blurring and visual artifacts in overlapping regions when the images are unprojected onto the mesh surface.

To this end, we introduce a novel framework that addresses both challenges by learning a **Material Latent** space, referred to as MATLAT, which substantially improves the quality of generated PBR textures. Specifically, we propose a two-stage pipeline: we first learn the material latent space by fine-tuning the pretrained VAE using PBR texture images, resulting in Material VAE (MATVAE), and then fine-tune a diffusion model to generate multi-view material images in the adapted latent space. Within this framework, we introduce the following two main components addressing the aforementioned challenges.

The first component is a latent-space adaptation module in MATVAE that extends the pretrained latent space to incorporate additional PBR channels—roughness and metallic—while preserving the pretrained prior. Most previous works [7, 12, 17, 21, 48, 59, 60] adopt a naïve approach that freezes the pretrained encoder and incorporates the additional PBR channels through zero-channel padding. While straightforward, this causes a severe distributional mismatch between the encoded PBR materials and the pretrained latent space, which leads to suboptimal performance during subsequent diffusion model fine-tuning. In contrast, our approach fine-tunes the pretrained encoder to effectively incorporate the additional channels of PBR material images while applying a distributional regularization that constrains deviations from the original latent distribution. This controlled adaptation effectively preserves the pretrained priors, stabilizes subsequent diffusion fine-tuning, and thereby better leverages these priors to produce higher-fidelity PBR textures. While similar latent-space extensions have been explored for transparent [55] or RGB-D image synthesis [27], this work is the *first* to adapt this idea to PBR texture generation, and we further identify crucial compo-

nents that make such adaptation effective in practice.

The second component is locality regularization in MATVAE, which establishes latent–image spatial alignment. This alignment is subsequently leveraged by correspondence-aware attention (CAA) [43] within the diffusion model. Previous work on multi-view generation [43] has shown that CAA effectively enforces correspondence across views in the pretrained RGB latent space when the latent-image mapping preserves spatial locality. While such locality largely holds for pretrained RGB encoder [17], it often breaks for additional material channels, leading to multi-view inconsistent images. To address this, we introduce *locality regularization*, applied during MATVAE fine-tuning, which explicitly enforces spatial alignment between latent tokens and image pixels. Specifically, we crop latent patches, decode them, and align the corresponding image regions with an ℓ_2 reconstruction loss, encouraging pixel–latent spatial locality.

In our experiments, we evaluate the quality of the generated PBR textures against comprehensive baselines, including models trained from scratch, SDS-based optimization methods, and multi-view diffusion models. Quantitative results with comprehensive evaluation metrics show that MATLAT outperforms baselines trained from scratch, which suffer from suboptimal quality due to limited PBR supervision, and SDS-based methods, which tend to produce over-saturated appearances and exhibit prohibitive runtimes. Notably, our method also outperforms multi-view diffusion baselines on most quantitative metrics, achieving new state-of-the-art performance. Additionally, we present systematic ablation studies that validate the effectiveness of each component of our framework, including the proposed latent-space adaptation in MATVAE, correspondence-aware attention, and locality regularization.

2. Related Work

2.1. PBR Texture Generation

Synthesizing PBR textures for 3D assets has emerged as an active area of research, driven by the growing integration of generative models into the 3D content creation pipeline. One line of research [41, 49] focuses on training models that directly generate 3D representations with associated material attributes from scratch. However, due to the limited availability and diversity of high-quality PBR texture data, these approaches exhibit suboptimal quality.

To address data scarcity, another class of approaches leverages pretrained diffusion models with expressive generative prior. Score Distillation Sampling (SDS) [36] leverages pretrained diffusion model to update the parameters of 3D representations and has been adapted to PBR texture generation [1, 10, 52, 58]. However, SDS tends to produce over-saturated colors, degrading fine details with costly gradient-based updates.

A promising direction is to generate multi-view PBR material images (*e.g.*, albedo, metallic, roughness) with diffusion models and then project them onto 3D meshes to obtain the texture maps. This approach exploits the expressive prior of pretrained diffusion models while enforcing multi-view consistency via cross-view attention or correspondence modules [7, 12, 17, 21, 48, 59, 60]. From this perspective, we adopt a multi-view image generation framework and present MATLAT which addresses two key challenges: (i) leveraging pretrained diffusion priors and (ii) ensuring multi-view consistency.

In the following subsections, we review previous works addressing these components, including approaches not limited to PBR material generation.

2.2. Leveraging Pretrained Diffusion Priors

Leveraging the generative prior of large-scale pretrained diffusion models is crucial for generating data in modalities with limited availability (*e.g.*, normal, depth, and alpha maps) [4, 13, 30, 53, 54]. A key challenge, however, lies in extending a diffusion model trained on latent RGB images to target modalities whose dimensionality differs due to the additional channels. A straightforward approach [17] processes the target modality image by splitting and padding its channels to form a three-channel tensor, feeding it to a frozen RGB-trained encoder, and then fine-tuning the diffusion model on the resulting latents. However, the encoded latent distribution generally exhibits a significant domain gap from the pretrained latent space since the target-modality channels (*e.g.*, roughness and metallic) are fed into an RGB encoder. This mismatch prevents leveraging the pretrained diffusion prior and leads to inefficient fine-tuning. To address this, LayerDiffuse [55] and Orchid [27] jointly fine-tune the VAE to align the latent representations of new modalities with the pretrained RGB latent space, reducing distributional discrepancies and improving the stability of subsequent diffusion fine-tuning. Inspired by this, in Sec. 3.1, we also propose to fine-tune the pretrained VAE while identifying the best practice that achieves superior performance compared to previous methods.

2.3. Multi-View-Consistent Generation

Beyond leveraging pretrained diffusion priors, maintaining multi-view consistency is crucial for high-quality PBR textures, as view misalignments during projection onto the mesh blur details in overlapping regions. Previous works address this challenge through dense multi-view attention [14, 17, 33, 40, 45], which concatenates tokens from all viewpoints to compute cross-view attention. While this design enables information sharing across views, it does not explicitly leverage geometric priors and often yields sub-optimal view consistency. A more effective approach is correspondence-aware attention (CAA) [43], which lever-

ages pixel-wise correspondence to enable geometry-guided feature sharing in the latent space. By restricting attention computation to geometrically corresponding regions, CAA improves cross-view consistency. However, CAA is most effective in the pretrained RGB latent space when latent-image spatial alignment is well preserved [22, 25, 29, 43]. To this end, in Sec. 3.2, we introduce *locality regularization*, applied during encoder fine-tuning to enforce spatial alignment between MATVAE latents and PBR images.

3. MATLAT: Material Latent Space

Our goal is to build a generative model that produces high-quality PBR textures for given meshes. In particular, we propose a model that leverages the priors of pretrained image diffusion models by generating PBR textures as multi-view images and projecting them onto the mesh. Specifically, let \mathcal{M} be a 3D mesh with surface \mathcal{S} , and let y be a text prompt specifying the target appearance. We denote a set of N camera viewpoints $\{c_i\}_{i=1}^N$, where each viewpoint c_i is defined by its rotation $\mathbf{R}_i \in \text{SO}(3)$ and translation $\mathbf{t}_i \in \mathbb{R}^3$. These parameters define an orthographic projection Π_i which maps the 3D surface \mathcal{S} onto the discrete $H \times W$ pixel grid $\Omega = \{1, \dots, H\} \times \{1, \dots, W\}$. Then, for each view c_i , our objective is to produce a five-channel PBR material image \mathbf{x}_i encoding albedo $\mathbf{a}_i \in \mathbb{R}^{H \times W \times 3}$, roughness $\mathbf{r}_i \in \mathbb{R}^{H \times W \times 1}$, and metallic $\mathbf{m}_i \in \mathbb{R}^{H \times W \times 1}$.

The key component of our framework is the representation of PBR material images, which we refer to as MATLAT. We design the latent space of PBR material images to effectively exploit the priors learned by pretrained latent image diffusion models while enhancing multi-view consistency. To effectively utilize pretrained diffusion priors, we introduce MATVAE that encodes PBR material images into a latent space aligned with the pretrained latent distribution via (i) residual prediction and (ii) KL regularization (Sec. 3.1). This adaptation minimizes distribution shift of the PBR material latents which further improves convergence in diffusion fine-tuning. To achieve multi-view consistency, we adopt correspondence-aware attention (CAA) [43] into the diffusion model. More importantly, we propose a novel locality regularization for MATVAE training to preserve latent-image spatial alignment and improve view consistency of the generated PBR material images (Sec. 3.2).

3.1. Material VAE (MATVAE)

We present MATVAE for encoding PBR material images while preserving the pretrained latent distribution. Unless stated otherwise, material images are rendered from a single viewpoint, and we omit the view subscript for simplicity. Before introducing our MATVAE, we first discuss Frozen VAE, a widely used approach for modeling material latents in PBR texture generation.

3.1.1. Prior Work: Frozen VAE [17]

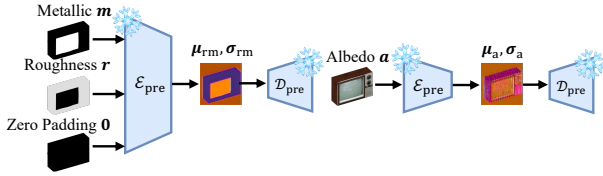


Figure 2. **Overview of Frozen VAE [17].** Zero-padded roughness–metallic maps and albedo image are encoded by the frozen VAE to produce (μ_{rm}, σ_{rm}) and (μ_a, σ_a) , respectively.

Leveraging the generative prior of pretrained diffusion models is critical for producing high-quality PBR material images. To this end, most previous works [7, 12, 17, 21, 48, 59, 60] adopt a naïve approach, which we term Frozen VAE, where the pretrained VAE is frozen and its encoder is reused to obtain latent representations for five-channel PBR input images. To match the three-channel input format of the pretrained VAE, the methods separately encode the albedo from the roughness and metallic channels, with the roughness and metallic concatenated with zero-padding before encoding. An overview of Frozen VAE design is shown in Fig. 2, where $(\mathcal{E}_{pre}, \mathcal{D}_{pre})$ denote the pretrained encoder and decoder, respectively. Formally, given a PBR material image $\mathbf{x} = [\mathbf{a}, \mathbf{r}, \mathbf{m}]$,

$$(\mu_{rm}, \sigma_{rm}) = \mathcal{E}_{pre}([\mathbf{r}, \mathbf{m}, \mathbf{0}]), (\mu_a, \sigma_a) = \mathcal{E}_{pre}(\mathbf{a}), \text{ and} \\ q(\mathbf{z}_{rm}|\mathbf{r}, \mathbf{m}) = \mathcal{N}(\mu_{rm}, \sigma_{rm}^2), q(\mathbf{z}_a|\mathbf{a}) = \mathcal{N}(\mu_a, \sigma_a^2),$$

where $\mathbf{0} \in \mathbb{R}^{H \times W \times 1}$ is the zero-padding channel. Here, $\mu_{\{\text{rm}, \text{a}\}}, \sigma_{\{\text{rm}, \text{a}\}}$ denote the mean and standard deviation for the roughness/metallic and albedo latents, respectively. The diffusion model is then fine-tuned using the concatenated latents $[\mathbf{z}_{rm}, \mathbf{z}_a]$.

While \mathbf{z}_a aligns closely with the pretrained latent space due to the semantic similarity of albedo to RGB images [17], \mathbf{z}_{rm} introduces a substantial domain gap, as roughness and metallic images exhibit distinct visual characteristics. This yields out-of-distribution latents that deviate from the representation space of pretrained diffusion models and, consequently, leads to suboptimal generation quality. Moreover, generating two separate latent codes doubles the inference cost of the diffusion model.

3.1.2. Residual Prediction and KL Regularization

To address this, we propose MATVAE, which adapts the pretrained latent space to encode PBR channels into a single latent code while preserving the pretrained diffusion prior. Motivated by the semantic similarity between albedo and RGB images observed in Frozen VAE, we reuse \mathcal{E}_{pre} to encode the albedo, *i.e.*, $q(\mathbf{z}_{base}|\mathbf{a}) = \mathcal{N}(\mu_{base}, \sigma_{base}^2)$, which serves as the base latent distribution. On the other hand, we introduce a learnable *residual encoder* \mathcal{E}_{res} to *inject* the roughness and metallic information. Specifically, as

shown in Fig. 3(a), the encoder predicts residual parameters $(\mu_{res}, \sigma_{res}) = \mathcal{E}_{res}(\mathbf{x})$, which adjust the base latent distribution:

$$\mathbf{z} \sim \mathcal{N}(\mu_{base} + \mu_{res}, \sigma_{base}^2 \odot \sigma_{res}^2) = q(\mathbf{z}|\mathbf{x}), \quad (1)$$

where \odot denotes element-wise multiplication. For notation convenience, we define $(\mu_{full}, \sigma_{full}) = (\mu_{base} + \mu_{res}, \sigma_{base} \odot \sigma_{res})$, denoting the mean and standard deviation of latent \mathbf{z} , respectively. We refer to the formulation above as residual prediction.

With a slight abuse of notation, let $\mathcal{E} = (\mathcal{E}_{pre}, \mathcal{E}_{res})$ denote the combination of the pretrained and residual encoders, and write $\mathcal{E}(\mathbf{x})$ for a latent sample \mathbf{z} drawn from the Gaussian distribution as in Eq. 1. During training, a learnable decoder \mathcal{D} maps the latent code \mathbf{z} back to the five-channel PBR material image, *i.e.*, $\hat{\mathbf{x}} = \mathcal{D}(\mathbf{z})$. Additionally, the pretrained encoder is kept frozen, and \mathcal{E}, \mathcal{D} are optimized using the following objectives:

$$\mathcal{L}_{d-rec} = \lambda_{d-rec} \cdot d(\mathbf{x}, \mathcal{D}(\mathcal{E}(\mathbf{x}))), \quad (2)$$

$$\mathcal{L}_{KL} = \lambda_{KL} \cdot \text{KL}(q(\mathbf{z}|\mathbf{x})\|\mathcal{N}(\mathbf{0}, I)), \quad (3)$$

$$\mathcal{L}_{disc} = \lambda_{disc} \cdot \mathcal{F}(\mathcal{D}(\mathcal{E}(\mathbf{x}))), \quad (4)$$

where $\lambda_{(\cdot)}$ are the weights for each loss term, \mathcal{F} denotes the discriminator used in the adversarial loss [15], and $d(\cdot, \cdot) \in \{\ell_2, \text{LPIPS}\}$ specifies the reconstruction distance metric.

While these objectives ensure faithful reconstruction and effective compression of PBR material images, the learned representation space can deviate from the pretrained latent distribution. To address this, we introduce a regularizer that penalizes the divergence between the learned latent distribution and that of the pretrained model:

$$\mathcal{L}_{reg} = \lambda_{reg} \cdot \text{KL}(\underbrace{q(\mathbf{z}|\mathbf{x})}_{\text{Learned}}\|\underbrace{q(\mathbf{z}_{base}|\mathbf{a})}_{\text{Pretrained}}). \quad (5)$$

The schematic of the KL regularization is presented in Fig. 3(b). This regularizer constrains the learned latent distribution to remain close to the pretrained latent space, ensuring compatibility with the diffusion prior.

Putting together, we introduce our Material VAE (MATVAE) which combines i) **residual prediction** (Eq. 1) and ii) **KL regularization** (Eq. 5). The schematic is shown in Fig. 3(c), with each component highlighted.

Connection to LayerDiffuse [55]. Residual prediction of VAE has also been explored for transparent image generation [55]. However, LayerDiffuse only predicts the latent mean, effectively treating the encoder as deterministic rather than stochastic, *i.e.*, $q(\mathbf{z}|\mathbf{x}) = \delta(\mathbf{z} - \mu_{full})$, which may disrupt the smooth latent representation of the pretrained VAE. Although an identity-consistency loss $\mathcal{L}_{id} = d(\mathbf{a}, \mathcal{D}_{pre}(\mathcal{E}(\mathbf{x})))$ is employed, it does *not* enforce distribution-level alignment with the pretrained latent

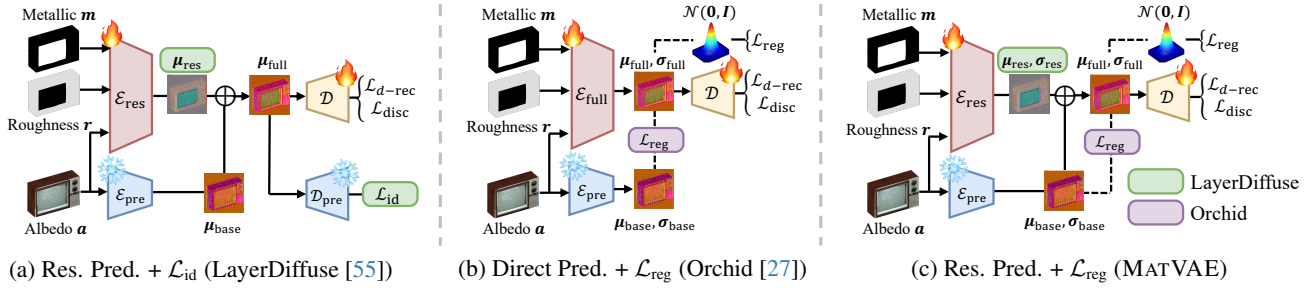


Figure 3. **Comparison of PBR Material Encoder Schemes.** (a) LayerDiffuse [55] uses residual prediction but only predicts the latent mean and enforces identity consistency via \mathcal{L}_{id} . (b) Orchid [27] uses direct prediction to output the full latent parameters ($\mu_{full}, \sigma_{full}$) and regularizes them with \mathcal{L}_{reg} . (c) MATVAE (ours) synergistically integrates residual prediction and KL regularization, enabling effective incorporation of PBR material images while preserving the pretrained latent space.

space. In contrast, we predict both the mean and standard deviation of the residual latent and introduce a KL regularizer that enforces distributional alignment.

Connection to Orchid [27]. We note that KL regularization has also been explored in Orchid [27] for depth and normal map generation. However, Orchid directly predicts ($\mu_{full}, \sigma_{full}$), while our MATVAE adopts a residual prediction, in which the final convolution layer of \mathcal{E}_{res} is initialized with zero weights, yielding zero residual predictions at the start of training and thus exactly reproducing the pretrained latent distribution. As observed in previous works [56], this initialization strategy stabilizes optimization and allows the latent space to be gradually adapted to the new modality.

Our Contributions. To our knowledge, this work is the first to introduce effective fine-tuning of latent embeddings for PBR texture generation. Also, in our experiments (Sec. 4), we ablate critical design choices and present a novel architecture with objectives distinct from prior approaches, demonstrating state-of-the-art performance.

3.2. Multi-View Consistent PBR Texture

In this section, we present two key components that together enforce multi-view consistency in PBR material generation.

3.2.1. Correspondence-Aware Attention

In addition to learning a valid material representation, PBR material images must satisfy multi-view consistency. However, the dense multi-view attention used in previous works [17, 40] do not leverage geometric priors, leading to inefficient computation and suboptimal results.

Formally, let $\mathbf{Z} \in \mathbb{R}^{Nhw \times d}$ denote the latent tokens derived from N viewpoints, each with spatial resolution $h \times w$, where d is the latent channel dimension. Then, a dense multi-view attention computes:

$$\text{softmax}(\mathbf{Q}\mathbf{K}^T/\sqrt{d})\mathbf{V}, \mathbf{Q} = \mathbf{W}_Q\mathbf{Z}, \mathbf{K} = \mathbf{W}_K\mathbf{Z}, \mathbf{V} = \mathbf{W}_V\mathbf{Z},$$

where $\mathbf{W}_{\{Q,K,V\}}$ denote the query, key, and value projections, respectively. Note that each token attends to all tokens in other views without geometric or visibility priors, forcing the network to learn correspondences implicitly. Consequently, the model converges slowly and produces view-inconsistent results.

To address the limitation of dense multi-view attention, correspondence-aware attention (CAA) [43] incorporates *explicit* point correspondences into the attention computation. In Fig. 4(a), we illustrate the CAA operation. Formally, for a pixel $u \in \Omega$ in view c_i , let the observed surface point $\mathbf{p}_i^{(u)} = \Pi_i^{-1}(u) \in \mathcal{S}$. Additionally, for every view $j \neq i$, we define the correspondence pixel as the nearest-neighbor discretization of the projection $\phi_{i \rightarrow j}(u) = \Pi_j(\mathbf{p}_i^{(u)})$ if the surface point is visible in view c_j . Then, the set of valid correspondences for u across the remaining $N - 1$ views is $\mathcal{C}(u) = \{\phi_{i \rightarrow j}(u) | j \neq i\}$. In practice, correspondences are implemented as a $K \times K$ local window centered at $\phi_{i \rightarrow j}(u)$. CAA is then computed by restricting computation to the correspondence set $\mathcal{C}(u)$:

$$\text{softmax}(\mathbf{Q}_u\mathbf{K}_{\mathcal{C}(u)}^T/\sqrt{d})\mathbf{V}_{\mathcal{C}(u)}, \quad (6)$$

where \mathbf{Q}_u is the query associated with token u , $\mathbf{K}_{\mathcal{C}(u)}$ and $\mathbf{V}_{\mathcal{C}(u)}$ are the keys and values of its correspondence set. Providing explicit correspondences in CAA strengthens cross-view alignment, yielding multi-view consistent PBR material images.

3.2.2. Locality Regularization

While CAA promotes cross-view feature exchange in latent space, our objective is to enforce multi-view consistency in the decoded pixel-space images. Hence, using CAA alone to achieve view consistency in pixel space requires spatial locality between latent tokens and their corresponding image pixels, *i.e.*, each image pixel is primarily decoded from its spatially local latent tokens. While this assumption holds for the pretrained encoder [22, 25, 29, 43],

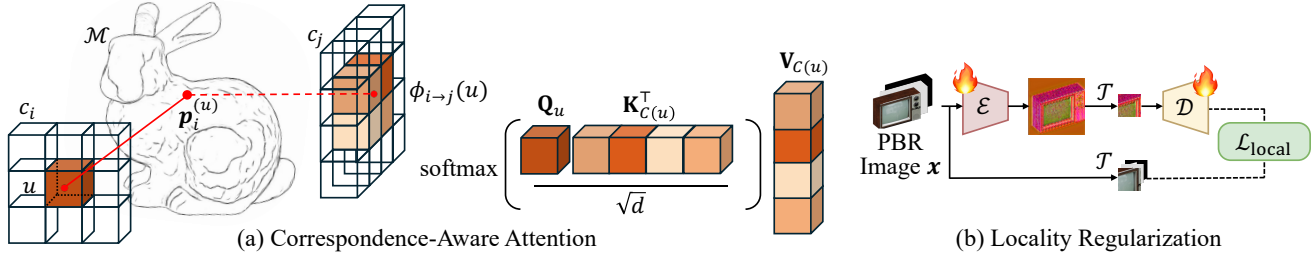


Figure 4. **Illustration of Correspondence-Aware Attention (CAA) and Locality Regularization.** (a) CAA restricts attention to geometrically corresponding tokens across views. (b) Locality regularizer enforces patch-wise reconstruction such that image pixels are decoded from spatially aligned latent tokens. Together, CAA and locality regularization enable multi-view consistent PBR texture generation.

MATVAE, which is fine-tuned to encode additional PBR channels under prior preservation regularization, may not preserve the latent-image locality. Consequently, applying CAA to MATVAE latents results in information exchange between geometrically unrelated tokens, degrading multi-view consistency.

To ensure latent-image spatial locality, we introduce a locality regularizer that enforces patch-wise reconstruction during MATVAE fine-tuning:

$$\mathcal{L}_{\text{local}} = \lambda_{\text{local}} \cdot d(\mathcal{T}(\mathbf{x}), \mathcal{D}(\mathcal{T}(\mathcal{E}(\mathbf{x})))) , \quad (7)$$

where $d(\cdot, \cdot) = \ell_2$ is the distance metric and \mathcal{T} is a random crop operator. We present a visualization of the regularizer in Fig. 4(b). This regularization enforces spatial locality by ensuring each image pixel is reconstructed mainly from aligned latent tokens.

Accordingly, we replace the reconstruction loss in Eq. 2 with the locality regularization, yielding the following MATVAE training objective:

$$\mathcal{L}_{\text{MATVAE}} = \mathcal{L}_{\text{local}} + \mathcal{L}_{\text{KL}} + \mathcal{L}_{\text{disc}} + \mathcal{L}_{\text{reg}} . \quad (8)$$

In Sec. 4, we validate that CAA and locality regularizer synergistically enhance multi-view consistency.

3.3. MATLAT Training Objective

We fine-tune a latent diffusion (velocity) model [11], denoted as u_θ , on multi-view PBR latents \mathbf{Z} obtained by rendering the mesh from N viewpoints and encoding each view with MATVAE. Additionally, we insert CAA modules into the attention blocks of the diffusion model, in addition to the original attention layers. Following Conditional Flow Matching (CFM) [32], we define a linear path between a data latent \mathbf{Z} and Gaussian noise $\epsilon \sim \mathcal{N}(\mathbf{0}, \mathbf{I})$: $\mathbf{Z}_t = (1 - t)\mathbf{Z} + t\epsilon$ for $t \in [0, 1]$. Our MATLAT is then trained using the CFM objective:

$$\mathcal{L}_{\text{MATLAT}} = \mathbb{E}_{t, \mathbf{Z}, \epsilon} \|u_\theta(\mathbf{Z}_t, t, y) - \mathbf{u}_t\|^2 , \quad (9)$$

where $\mathbf{u}_t = \epsilon - \mathbf{Z}$ is the instantaneous velocity, and y is the conditioning text caption.

4. Experiments

In this section, we present experimental results on PBR texture generation. We first describe the experimental setup (Sec. 4.1), followed by ablation studies that validate the effectiveness of each component (Sec. 4.2). Finally, we report quantitative comparisons against external baselines (Sec. 4.3). In the appendix, we present (i) implementation and experiment details and (ii) additional qualitative results.

4.1. Experiment Setup

We fine-tune MATLAT from the pretrained VAE and diffusion model of STABLE DIFFUSION 3.5-MEDIUM, using 40,723 PBR-textured assets from Objaverse-XL [8] paired with captions from Bootstrap3D [42] and Cap3D [34] as training data. During training, we render 26 images from fixed viewpoints for each 3D mesh.

For generation, we use six canonical views (front, back, left, right, top, and bottom) following previous works [17, 21]. For evaluation, we follow PacTure [12] and use 128 meshes not included in the training set, using $N = 20$ camera views per mesh: eight views uniformly spaced in azimuth at 0° elevation, six at 30° , four at 45° , and two polar views at $\pm 90^\circ$. For each view, we render (i) albedo, roughness, and metallic images and (ii) a shaded RGB image under randomly sampled HDR environment maps. The reference images are rendered using the same set of 20 camera views and the identical HDR environment maps with the ground-truth PBR textures.

Evaluation Metrics. Following the previous work [12], for shaded and albedo images, we report FID [18] and KID [3] between generated and reference sets to evaluate fidelity and diversity, with FID computed in the CLIP embedding space [37]. We additionally measure text-image alignment using CLIP cosine similarity between rendered images and the input prompt. For roughness and metallic images, we compute the root mean square error (RMSE) against the corresponding ground-truth images. However, these metrics do not reflect the consistency of the generated multi-view material images. To this end, we introduce c-PSNR, which computes the PSNR between each pixel u and its corresponding points $\mathcal{C}(u)$. A detailed formulation

Table 1. **Quantitative Results of Ablation Study.** Best scores are **bold**, and the runner-up scores are underlined.

Id	Methods	Shaded			Albedo			Rough.	Metal.	c-PSNR \uparrow	Time \downarrow
		FID _{CLIP} \downarrow	KID \downarrow	CLIP \uparrow	FID _{CLIP} \downarrow	KID \downarrow	CLIP \uparrow	RMSE \downarrow	RMSE \downarrow		
1	Frozen VAE [17]	3.419	1.052	<u>0.318</u>	4.926	1.560	0.315	0.193	0.251	19.869	111s
2	Res. Pred. + \mathcal{L}_{reg} (Ours)	3.083	1.327	<u>0.318</u>	4.599	1.574	<u>0.314</u>	0.158	<u>0.134</u>	21.934	34s
3	\perp Res. Pred. + \mathcal{L}_{id} [55]	3.210	1.090	0.317	4.871	1.525	0.312	0.165	0.128	20.977	34s
4	\perp Direct Pred. + \mathcal{L}_{reg} [27]	3.192	1.146	0.319	4.768	<u>1.472</u>	0.312	0.161	0.170	<u>21.468</u>	34s
5	\perp w/o \mathcal{L}_{local}	3.419	1.611	0.316	5.873	4.122	0.312	0.154	0.182	19.437	34s
6	\perp w/o CAA	<u>3.110</u>	<u>1.088</u>	0.317	<u>4.732</u>	1.388	0.312	<u>0.155</u>	0.151	18.687	38s

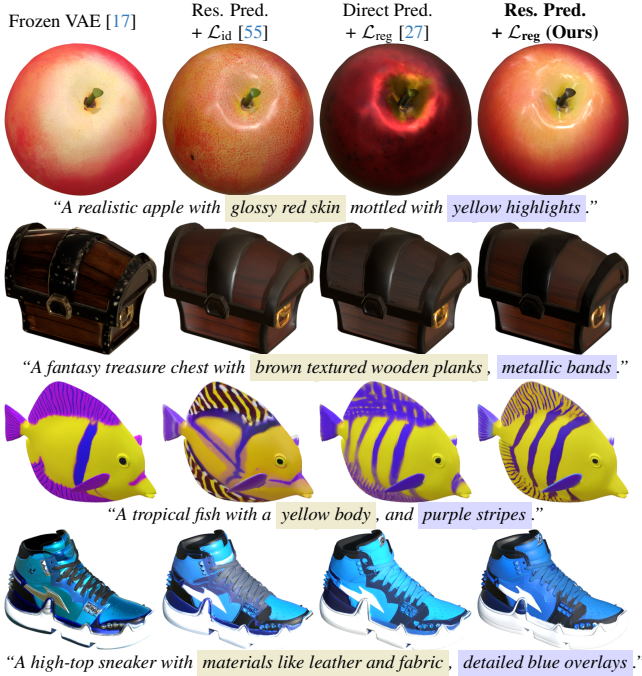


Figure 5. **Qualitative Comparisons across Each Component.** Combining residual prediction with \mathcal{L}_{reg} effectively preserves the pretrained latent distribution and yields high-quality PBR textures.

is provided in the appendix. Lastly, we report the runtime in seconds required to generate a PBR texture.

4.2. Ablation Studies

In this section, we validate the effectiveness of each component introduced in Sec. 3. Specifically, we report the following cases discussed in Sec. 3.1:

- **Frozen VAE [17]:** Directly uses the pretrained VAE.
- **Res. Pred. + \mathcal{L}_{reg} (Ours):** Fine-tunes the encoder using residual prediction with KL regularization (MATLAT).
- **Res. Pred. + \mathcal{L}_{id} [55]:** Replaces KL regularization of MATLAT with identity loss, as in LayerDiffuse [55].
- **Dense. Pred. + \mathcal{L}_{reg} [27]:** Replaces residual prediction of MATLAT with dense prediction, as in Orchid [27].

For each case, the pretrained VAE and diffusion model are fine-tuned for 200K and 20K training steps, respectively. As Frozen VAE does not require encoder fine-tuning, we al-

locate more diffusion fine-tuning steps (45K) to match the overall training compute. Additionally, all cases share the same diffusion architecture and training scheme to MATLAT, with both CAA and the locality regularization enabled. To further analyze these components, we additionally consider the components discussed in Sec. 3.2:

- **w/o \mathcal{L}_{local} :** Localization regularization removed from MATLAT encoder fine-tuning stage.
- **w/o CAA:** CAA module removed from MATLAT, replaced with dense view attention.

Results. In Tab. 1, we present the quantitative results of our ablation studies. First, we observe that Frozen VAE (row 1) consistently yields higher FID scores than our MATLAT (row 2) for both shaded and albedo images, while achieving slightly better or comparable KID scores. Moreover, the noticeable gap in the RMSE of roughness and metallic images indicates that the domain gap introduced by the additional channels leads to out-of-distribution latents, which in turn degrades generation performance. Additionally, we observe that MATLAT outperforms the other encoder fine-tuning schemes (rows 3-4) adopted in previous works [27, 55] in FID scores of both shaded and albedo images and comparable scores in KID and RSME scores, except in KID of shaded images where our method underperforms. Qualitatively, Fig. 5 shows that combining residual prediction with \mathcal{L}_{reg} enables our MATLAT to produce PBR textures with superior text-alignment (e.g., the glossy apple surface in row 1) and sharper fine details (e.g., the fish fin in row 3).

Next, we ablate the two components introduced in Sec. 3.2: CAA and locality regularization \mathcal{L}_{local} . When CAA is applied alone without \mathcal{L}_{local} (row 5), we observe consistent drops across most metrics, including a noticeable decrease in c-PSNR compared to MATLAT. Without the regularizer, the latent-pixel mapping is not enforced to be spatially local and applying CAA can propagate information across unrelated regions leading to performance drops. On the other hand, when CAA is removed and \mathcal{L}_{local} is applied alone (row 6), the model does not exhibit noticeable performance drops on most metrics, but still shows inferior c-PSNR, as it must infer correspondences implicitly via dense multi-view attention, resulting in weaker cross-

Table 2. **Quantitative Comparisons of PBR Texture Generation Methods.** Best scores are **bold**, and the runner-up scores are underlined.

Method	Type	Shaded			Albedo			Rough.	Metal.	Time ↓
		FID _{CLIP} ↓	KID ↓	CLIP ↑	FID _{CLIP} ↓	KID ↓	CLIP ↑	RMSE ↓	RMSE ↓	
MeshGen [7]	SC	8.637	11.105	0.282	11.322	16.193	0.282	0.143	0.201	195s
TexGaussian [49]	SC	6.025	3.571	0.301	12.119	9.381	0.299	<u>0.145</u>	0.243	73s
Paint-it [52]	SDS	8.547	5.382	0.309	13.063	10.665	0.299	0.168	0.200	1260s
DreamMat [58]	SDS	<u>5.422</u>	<u>2.668</u>	0.311	<u>9.621</u>	<u>6.002</u>	0.311	0.167	0.165	2400s
FlashTex [10]	SDS	7.119	5.354	0.305	12.320	10.441	0.298	0.143	0.186	285s
MaterialAnything [21]	MV	6.582	5.287	<u>0.312</u>	12.691	9.325	0.317	0.233	0.200	500s
MaterialMVP [17]	MV	6.309	5.744	0.294	9.630	8.811	0.290	0.175	0.133	<u>35s</u>
MATLAT (Ours)	MV	3.083	1.327	0.318	4.599	1.574	<u>0.314</u>	0.158	<u>0.134</u>	34s



Figure 6. **Qualitative Results of MATLAT.** MATLAT produces realistic textures with strong text-alignment across diverse material types.

view alignment. Our MATLAT, which combines CAA with $\mathcal{L}_{\text{local}}$, enforces cross-view feature exchange along geometrically valid correspondences and achieves the highest c-PSNR without performance degradation.

4.3. Comparison to Other Baselines

In this section, we compare MATLAT to baselines that address PBR texture generation. Due to substantial differences in training schemes, pretrained models, datasets, and implementation details across the literature, a strictly unified experimental setting is practically infeasible. We therefore use the official pretrained model of each baseline with its default configuration to generate textured meshes, and then render and evaluate all methods under the same setup.

Baselines. We compare MATLAT against the following baseline categories: (i) models trained from scratch to predict PBR textures (**SC**) [7, 49], (ii) SDS-based optimization methods (**SDS**) [10, 52, 58], and (iii) multi-view diffusion models (**MV**) [17, 21].

Results. In Tab. 2, we present quantitative results of the baselines and MATLAT. We observe that models trained from scratch (SC) [7, 49] generally exhibit suboptimal performances compared to MATLAT, indicating low-fidelity PBR textures caused by suboptimal training under limited high-quality PBR supervision. While SDS-based methods (SDS) [10, 52, 58] lead to improved overall metrics than SC-based methods, aside from DreamMat which incurs a prohibitive runtime of approximately **40 minutes**, we observe only marginal improvements. Lastly, MATLAT effectively leverages the pretrained prior while preserving multi-

view consistency, achieves the *best* performance on shaded and albedo images across all baselines, with the exception of the albedo CLIP score which is marginally behind MaterialAnything [21].

We present qualitative results of MATLAT in Fig. 6, which produces high-quality, physically plausible textures across diverse material types. We provide comprehensive qualitative comparisons between the baselines and MATLAT on the project page.

5. Conclusion

In this work, we presented MATLAT, a two-stage pipeline that leverages the priors of pretrained image diffusion models for PBR texture generation. Directly extending image diffusion models to PBR material images is challenging due to the domain gap introduced by roughness and metallic channels. To address this, we introduce effective latent-space adaptation, MATVAE, which incorporates PBR material images into the pretrained latent distribution, together with locality regularization that enhances multi-view consistency during correspondence-aware attention computation. Experimental results show that our MATLAT, a diffusion model fine-tuned on our material latent space, achieves superior performance in PBR texture generation, with ablations validating the effectiveness of each component.

Potential Negative Societal Impacts. The proposed framework could be misused to generate hyper-realistic synthetic 3D assets that facilitate misinformation or deceptive digital content.

References

- [1] Mishan Aliev, Dmitry Baranchuk, and Kirill Struminsky. Castex: Cascaded text-to-texture synthesis via explicit texture maps and physically-based shading. 2025. 2
- [2] Raphael Bensadoun, Yanir Kleiman, Idan Azuri, Omri Harosh, Andrea Vedaldi, Natalia Neverova, and Oran Gafni. Meta 3d texturegen: Fast and consistent texture generation for 3d objects. *arXiv preprint arXiv:2407.02430*, 2024. 13
- [3] Mikołaj Bińkowski, Danica J. Sutherland, Michael Arbel, and Arthur Gretton. Demystifying mmd gans. In *ICLR*, 2018. 6
- [4] Kwon Byung-Ki, Qi Dai, Lee Hyoseok, Chong Luo, and Tae-Hyun Oh. Jointdit: Enhancing rgb-depth joint modeling with diffusion transformers. In *ICCV*, 2025. 3
- [5] Dave Zhenyu Chen, Yawar Siddiqui, Hsin-Ying Lee, Sergey Tulyakov, and Matthias Nießner. Text2tex: Text-driven texture synthesis via diffusion models. In *ICCV*, 2023. 1
- [6] Rui Chen, Yongwei Chen, Ningxin Jiao, and Kui Jia. Fantasia3d: Disentangling geometry and appearance for high-quality text-to-3d content creation. In *ICCV*, 2023. 1
- [7] Zilong Chen, Yikai Wang, Wenqiang Sun, Feng Wang, Yiwen Chen, and Huaping Liu. Meshgen: Generating pbr textured mesh with render-enhanced auto-encoder and generative data augmentation. In *CVPR*, 2025. 1, 2, 3, 4, 8, 13, 14
- [8] Matt Deitke, Ruoshi Liu, Matthew Wallingford, Huong Ngo, Oscar Michel, Aditya Kusupati, Alan Fan, Christian Laforte, Vikram Voleti, Samir Yitzhak Gadre, Eli VanderBilt, Aniruddha Kembhavi, Carl Vondrick, Georgia Gkioxari, Kiana Ehsani, Ludwig Schmidt, and Ali Farhadi. Objaverse-xl: A universe of 10m+ 3d objects. In *NeurIPS*, 2023. 1, 6, 14
- [9] Matt Deitke, Dustin Schwenk, Jordi Salvador, Luca Weihs, Oscar Michel, Eli VanderBilt, Ludwig Schmidt, Kiana Ehsani, Aniruddha Kembhavi, and Ali Farhadi. Objaverse: A universe of annotated 3d objects. In *CVPR*, pages 13142–13153, 2023. 1
- [10] Kangle Deng, Timothy Omernick, Alexander Weiss, Deva Ramanan, Jun-Yan Zhu, Tinghui Zhou, and Maneesh Agrawala. Flashtex: Fast relightable mesh texturing with lightcontrolnet. In *ECCV*, 2024. 2, 8, 14
- [11] Patrick Esser, Sumith Kulal, Andreas Blattmann, Rahim Entezari, Jonas Müller, Harry Saini, Yam Levi, Dominik Lorenz, Axel Sauer, Frederic Boesel, Dustin Podell, Tim Dockhorn, Zion English, Kyle Lacey, Alex Goodwin, Yan-nik Marek, and Robin Rombach. Scaling rectified flow transformers for high-resolution image synthesis. *arXiv preprint arXiv:2403.03206*, 2024. 6, 13
- [12] Fan Fei, Jiajun Tang, Fei-Peng Tian, Boxin Shi, and Ping Tan. Pature: Efficient pbr texture generation on packed views with visual autoregressive models. *arXiv preprint arXiv:2505.22394*, 2025. 2, 3, 4, 6
- [13] Xiao Fu, Wei Yin, Mu Hu, Kaixuan Wang, Yuexin Ma, Ping Tan, Shaojie Shen, Dahua Lin, and Xiaoxiao Long. Geowizard: Unleashing the diffusion priors for 3d geometry estimation from a single image. In *ECCV*, 2024. 3
- [14] Ruiqi Gao, Aleksander Holynski, Philipp Henzler, Arthur Brussee, Ricardo Martin-Brualla, Pratul Srinivasan, Jonathan T. Barron, and Ben Poole. Cat3d: Create anything in 3d with multi-view diffusion models. In *NeurIPS*, 2024. 3
- [15] Ian J. Goodfellow, Jean Pouget-Abadie, Mehdi Mirza, Bing Xu, David Warde-Farley, Sherjil Ozair, Aaron Courville, and Yoshua Bengio. Generative adversarial networks. In *NeurIPS*, 2014. 4
- [16] Mohamed Hassan, Yunrong Guo, Tingwu Wang, Michael Black, Sanja Fidler, and Xue Bin Peng. Synthesizing physical character-scene interactions. In *SIGGRAPH*, 2023. 1
- [17] Zebin He, Mingxin Yang, Shuhui Yang, Yixuan Tang, Tao Wang, Kaihao Zhang, Guanying Chen, Yuhong Liu, Jie Jiang, Chunchao Guo, and Wenhan Luo. Materialmvp: Illumination-invariant material generation via multi-view pbr diffusion. In *ICCV*, 2025. 2, 3, 4, 5, 6, 7, 8, 13, 14
- [18] Martin Heusel, Hubert Ramsauer, Thomas Unterthiner, Bernhard Nessler, and Sepp Hochreiter. Gans trained by a two time-scale update rule converge to a local nash equilibrium. In *NeurIPS*, 2017. 6
- [19] Jonathan Ho and Tim Salimans. Classifier-free diffusion guidance. *arXiv preprint arXiv:2207.12598*, 2022. 13
- [20] Edward J Hu, Yelong Shen, Phillip Wallis, Zeyuan Allen-Zhu, Yuanzhi Li, Shean Wang, Lu Wang, Weizhu Chen, et al. Lora: Low-rank adaptation of large language models. *ICLR*, 1(2):3, 2022. 13
- [21] Xin Huang, Tengfei Wang, Ziwei Liu, and Qing Wang. Material anything: Generating materials for any 3d object via diffusion. In *CVPR*, 2024. 2, 3, 4, 6, 8, 14
- [22] Zehuan Huang, Yuan-Chen Guo, Haoran Wang, Ran Yi, Lizhuang Ma, Yan-Pei Cao, and Lu Sheng. Mv-adapter: Multi-view consistent image generation made easy. In *ICCV*, 2025. 3, 5, 13
- [23] Lukas Höllein, Ang Cao, Andrew Owens, Justin Johnson, and Matthias Nießner. Text2room: Extracting textured 3d meshes from 2d text-to-image models. In *ICCV*, 2023. 1
- [24] Heewoo Jun and Alex Nichol. Shape: Generating conditional 3d implicit functions. *arXiv preprint arXiv:2305.02463*, 2023. 1
- [25] Yash Kant, Ziyi Wu, Michael Vasilkovsky, Guocheng Qian, Jian Ren, Riza Alp Guler, Bernard Ghanem, Sergey Tulyakov, Igor Gilitschenski, and Aliaksandr Siarohin. Spad: Spatially aware multiview diffusers. In *CVPR*, 2024. 3, 5
- [26] Jaihoon Kim, Juil Koo, Kyeongmin Yeo, and Minhyuk Sung. Synctweedies: A general generative framework based on synchronized diffusions. In *NeurIPS*, 2024. 1, 2
- [27] Akshay Krishnan, Xinchun Yan, Vincent Casser, and Abhijit Kundu. Orchid: Image latent diffusion for joint appearance and geometry generation. In *ICCV*, 2025. 2, 3, 5, 7
- [28] Haoran Li, Haolin Shi, Wenli Zhang, Wenjun Wu, Yong Liao, Lin Wang, Lik-Hang Lee, and Peng Yuan Zhou. Dreamscene: 3d gaussian-based text-to-3d scene generation via formation pattern sampling. In *ECCV*, 2024. 1
- [29] Peng Li, Yuan Liu, Xiaoxiao Long, Feihu Zhang, Cheng Lin, Mengfei Li, Xingqun Qi, Shanghang Zhang, Wenhan Luo, Ping Tan, Wenping Wang, Qifeng Liu, and Yike Guo. Era3d: High-resolution multiview diffusion using efficient row-wise attention. In *NeurIPS*, 2024. 3, 5

- [30] Zhibing Li, Tong Wu, Jing Tan, Mengchen Zhang, Jiaqi Wang, and Dahua Lin. Idarb: Intrinsic decomposition for arbitrary number of input views and illuminations. In *ICLR*, 2025. 3
- [31] Chen-Hsuan Lin, Jun Gao, Luming Tang, Towaki Takikawa, Xiaohui Zeng, Xun Huang, Karsten Kreis, Sanja Fidler, Ming-Yu Liu, and Tsung-Yi Lin. Magic3d: High-resolution text-to-3d content creation. In *CVPR*, 2023. 2
- [32] Yaron Lipman, Ricky T. Q. Chen, Heli Ben-Hamu, Maximilian Nickel, and Matt Le. Flow matching for generative modeling. In *ICLR*, 2023. 6, 13
- [33] Xiaoxiao Long, Yuan-Chen Guo, Cheng Lin, Yuan Liu, Zhiyang Dou, Lingjie Liu, Yuexin Ma, Song-Hai Zhang, Marc Habermann, Christian Theobalt, and Wenping Wang. Wonder3d: Single image to 3d using cross-domain diffusion. In *CVPR*, 2024. 3
- [34] Tiange Luo, Chris Rockwell, Honglak Lee, and Justin Johnson. Scalable 3d captioning with pretrained models. In *NeurIPS*, 2023. 6, 14
- [35] Mathis Petrovich, Michael J. Black, and Gül Varol. Tmr: Text-to-motion retrieval using contrastive 3d human motion synthesis. In *ICCV*, 2023. 1
- [36] Ben Poole, Ajay Jain, Jonathan T. Barron, and Ben Mildenhall. Dreamfusion: Text-to-3d using 2d diffusion. In *ICLR*, 2023. 1, 2
- [37] Alec Radford, Jong Wook Kim, Chris Hallacy, Aditya Ramesh, Gabriel Goh, Sandhini Agarwal, Girish Sastry, Amanda Askell, Pamela Mishkin, Jack Clark, Gretchen Krueger, and Ilya Sutskever. Learning transferable visual models from natural language supervision. In *International Conference on Machine Learning*, 2021. 6
- [38] Elad Richardson, Gal Metzer, Yuval Alaluf, Raja Giryes, and Daniel Cohen-Or. Texture: Text-guided texturing of 3d shapes. In *SIGGRAPH*, 2023. 1
- [39] Christoph Schuhmann, Romain Beaumont, Richard Vencu, Cade Gordon, Ross Wightman, Mehdi Cherti, Theo Coombes, Aarush Katta, Clayton Mullis, Mitchell Wortsman, Patrick Schramowski, Srivatsa Kundurthy, Katherine Crowson, Ludwig Schmidt, Robert Kaczmarczyk, and Jenia Jitsev. Laion-5b: An open large-scale dataset for training next generation image-text models. In *NeurIPS*, 2022. 2
- [40] Yichun Shi, Peng Wang, Jianglong Ye, Mai Long, Kejie Li, and Xiao Yang. Mvdream: Multi-view diffusion for 3d generation. In *ICLR*, 2024. 3, 5
- [41] Yawar Siddiqui, Tom Monnier, Filippos Kokkinos, Mahendra Kariya, Yanir Kleiman, Emilien Garreau, Oran Gafni, Natalia Neverova, Andrea Vedaldi, Roman Shapovalov, and David Novotny. Meta 3d assetgen: Text-to-mesh generation with high-quality geometry, texture, and pbr materials. In *NeurIPS*, 2024. 2
- [42] Zeyi Sun, Tong Wu, Pan Zhang, Yuhang Zang, Xiaoyi Dong, Yuanjun Xiong, Dahua Lin, and Jiaqi Wang. Bootstrap3d: Improving multi-view diffusion model with synthetic data. In *ICCV*, 2025. 6, 14
- [43] Shitao Tang, Fuyang Zhang, Jiacheng Chen, Peng Wang, and Yasutaka Furukawa. Mvdifusion: Enabling holistic multi-view image generation with correspondence-aware diffusion. In *NeurIPS*, 2023. 2, 3, 5
- [44] Guy Tevet, Sigal Raab, Brian Gordon, Yonatan Shafir, Daniel Cohen-Or, and Amit H. Bermano. Human motion diffusion model. In *ICLR*, 2023. 1
- [45] Peng Wang and Yichun Shi. Imagedream: Image-prompt multi-view diffusion for 3d generation. *arXiv preprint arXiv:2312.02201*, 2023. 3
- [46] Yitong Wang, Xudong Xu, Li Ma, Haoran Wang, and Bo Dai. Boosting 3d object generation through pbr materials. In *SIGGRAPH*, 2024. 1
- [47] Zhengyi Wang, Cheng Lu, Yikai Wang, Fan Bao, Chongxuan Li, Hang Su, and Jun Zhu. Prolificdreamer: High-fidelity and diverse text-to-3d generation with variational score distillation. In *NeurIPS*, 2023. 2
- [48] Xiaokang Wei, Bowen Zhang, Xianghui Yang, Yuxuan Wang, Chunchao Guo, Xi Zhao, and Yan Luximon. Pbr3dgen: A vlm-guided mesh generation with high-quality pbr texture. *arXiv preprint arXiv:2503.11368*, 2025. 2, 3, 4
- [49] Bojun Xiong, Jialun Liu, Jiakui Hu, Chenming Wu, Jinbo Wu, Xing Liu, Chen Zhao, Errui Ding, and Zhouhui Lian. Texgaussian: Generating high-quality pbr material via octree-based 3d gaussian splatting. In *CVPR*, 2025. 2, 8, 14
- [50] Kyeongmin Yeo, Jaihoon Kim, and Minhyuk Sung. Stochsync: Stochastic diffusion synchronization for image generation in arbitrary spaces. In *ICLR*, 2025. 1, 2
- [51] Taoran Yi, Jiemin Fang, Junjie Wang, Guanjun Wu, Lingxi Xie, Xiaopeng Zhang, Wenyu Liu, Qi Tian, and Xinggang Wang. Gaussiandreamer: Fast generation from text to 3d gaussians by bridging 2d and 3d diffusion models. In *CVPR*, 2024. 1
- [52] Kim Youwang, Tae-Hyun Oh, and Gerard Pons-Moll. Paint-it: Text-to-texture synthesis via deep convolutional texture map optimization and physically-based rendering. In *CVPR*, 2024. 2, 8, 14
- [53] Fanghua Yu, Jinjin Gu, Jinfan Hu, Zheyuan Li, and Chao Dong. Unicon: Unidirectional information flow for effective control of large-scale diffusion models. In *ICLR*, 2025. 3
- [54] Zheng Zeng, Valentin Deschaintre, Iliyan Georgiev, Yannick Hold-Geoffroy, Yiwei Hu, Fujun Luan, Ling-Qi Yan, and Miloš Hašan. RGB \leftrightarrow X: Image decomposition and synthesis using material- and lighting-aware diffusion models. In *SIGGRAPH*, 2024. 3
- [55] Lvmin Zhang and Maneesh Agrawala. Transparent image layer diffusion using latent transparency. In *SIGGRAPH*, 2024. 2, 3, 4, 5, 7
- [56] Lvmin Zhang, Anyi Rao, and Maneesh Agrawala. Adding conditional control to text-to-image diffusion models. In *ICCV*, 2023. 5
- [57] Qihang Zhang, Chaoyang Wang, Aliaksandr Siarohin, Peiye Zhuang, Yinghao Xu, Ceyuan Yang, Dahua Lin, Bolei Zhou, Sergey Tulyakov, and Hsin-Ying Lee. Scenewiz3d: Towards text-guided 3d scene composition. In *CVPR*, 2024. 1
- [58] Yuqing Zhang, Yuan Liu, Zhiyu Xie, Lei Yang, Zhongyuan Liu, Mengzhou Yang, Runze Zhang, Qilong Kou, Cheng Lin, Wenping Wang, and Xiaogang Jin. Dreammat: High-quality pbr material generation with geometry- and light-aware diffusion models. In *SIGGRAPH*, 2024. 2, 8, 14

- [59] Lingting Zhu, Jingrui Ye, Runze Zhang, Zeyu Hu, Yingda Yin, Lanjong Li, Jinnan Chen, Shengju Qian, Xin Wang, Qingmin Liao, and Lequan Yu. Muma: 3d pbr texturing via multi-channel multi-view generation and agentic post-processing. *arXiv preprint arXiv:2503.18461*, 2025. [2](#), [3](#), [4](#)
- [60] Shenhao Zhu, Lingteng Qiu, Xiaodong Gu, Zhengyi Zhao, Chao Xu, Yuxiao He, Zhe Li, Xiaoguang Han, Yao Yao, Xun Cao, Siyu Zhu, Weihao Yuan, Zilong Dong, and Hao Zhu. Mcmat: Multiview-consistent and physically accurate pbr material generation. *arXiv preprint arXiv:2412.14148*, 2024. [2](#), [3](#), [4](#)

Appendix

In this appendix, we present technical discussions (Sec. A), implementation details (Sec. B), and qualitative results (Sec. C).

A. Technical Discussions

In this section, we detail our correspondence-PSNR metric (Sec. A.1) and provide qualitative analyses of VAE prediction types (Sec. A.2) and locality regularization (Sec. A.3).

A.1. Correspondence-PSNR

To quantify the multi-view consistency of the generated PBR material images, we introduced a correspondence-PSNR (c-PSNR) metric in Sec. 4 of the main paper.

Specifically, given a set of N generated view images $\{\mathbf{x}_i\}_{i=1}^N$ and a 3D mesh, for each pixel $u \in \Omega$ in the i -th view, the set of corresponding pixels in the j -th view is denoted as $\mathcal{C}_{i \rightarrow j}(u)$. We then compute the MSE (mean squared error) as follows:

$$\text{MSE} = \frac{1}{M} \sum_{i=1}^N \sum_{j \neq i} \sum_{\substack{u \in \Omega, \\ v \in \mathcal{C}_{i \rightarrow j}(u)}} \|\mathbf{x}_i(u) - \mathbf{x}_j(v)\|^2, \quad (10)$$

where $M = \sum_{i=1}^N \sum_{j \neq i} \sum_{u \in \Omega} |\mathcal{C}_{i \rightarrow j}(u)|$ is the total number of correspondence pairs. Accordingly, we define the correspondence-PSNR as

$$\text{c-PSNR} = 10 \log_{10}(1/\text{MSE}),$$

which provides a measure of the discrepancy across all geometric correspondences between views. As shown in Tab. 1, MATLAT achieves higher c-PSNR than methods without CAA, indicating more consistent PBR material images across views.

A.2. Additional Analysis of Direct and Residual Prediction

As discussed in Sec. 3.1 of the main paper, residual prediction can be more effective than direct prediction for VAE fine-tuning. In this section, we present an empirical comparison of residual and direct prediction for VAE during the early stage of fine-tuning, highlighting their optimization behavior and stability.

We present a qualitative comparison in Fig. 7. The left column shows the ground-truth albedo, roughness, and metallic maps. The middle and right columns show reconstruction error maps, computed between the ground-truth images and the outputs of VAEs fine-tuned with direct prediction and residual prediction (Ours), respectively, where brighter regions indicate higher errors. All results are evaluated at the same early fine-tuning step (after 10k iterations) for a fair comparison.

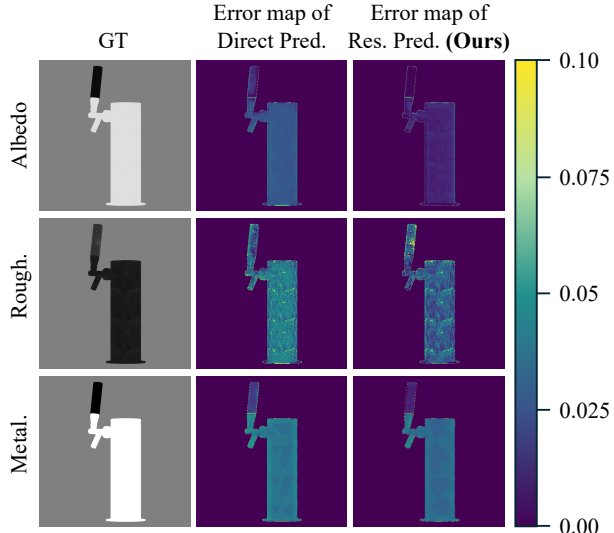


Figure 7. **Reconstruction Errors for Direct and Residual Prediction.** We show the albedo, roughness, and metallic reconstruction errors at an early training stage (10k iterations) for direct and residual prediction (**Ours**). Residual prediction preserves the pretrained latent representation, achieving superior albedo reconstruction quality (darker regions indicate lower errors).

Note that the reconstruction error of the albedo map under residual prediction is smaller than that under direct prediction. This is because residual prediction initializes the final layer weights of the offset encoder to zero, producing zero residuals at the start of training and thereby preserving the original latent representation. In contrast, direct prediction is not constrained to remain aligned with the pretrained latent space and, even after several update steps, already exhibits noticeable degradation in albedo reconstruction quality. While the errors for roughness and metallic maps remain comparable between the two schemes, we empirically observe that the improved stability of residual prediction on albedo images translates into better downstream generation performance, as reported in Tab. 1 of the main paper.

A.3. Additional Analysis of Locality Regularization

As discussed in Sec. 3.2 of the main paper, applying locality regularization $\mathcal{L}_{\text{local}}$ improves latent-image spatial alignment and leads to superior performance when combined with CAA. In Fig. 8, we visualize the reconstruction error of cropped patches using a VAE fine-tuned with and without $\mathcal{L}_{\text{local}}$ to further analyze the effect of the regularizer. Specifically, we show cropped patches from the albedo, roughness, and metallic images, together with their reconstruction error maps, $\|\mathbf{x} - \mathcal{D}(\mathcal{E}(\mathbf{x}))\|^2$, computed at an 8×8 latent resolution for VAEs fine-tuned without and with $\mathcal{L}_{\text{local}}$, where brighter regions indicate higher errors.

Note that applying $\mathcal{L}_{\text{local}}$ significantly reduces the reconstruction error, indicating that the learned latent representa-

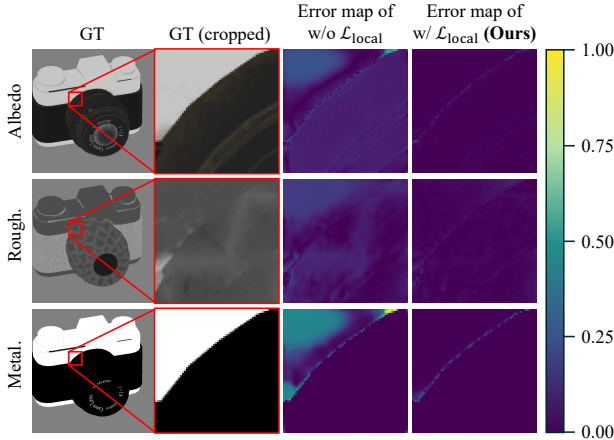


Figure 8. **Visualization of Reconstruction Error Maps on Cropped Patches.** We show albedo, roughness, and metallic reconstruction error maps for MATVAE trained with and without $\mathcal{L}_{\text{local}}$. Applying $\mathcal{L}_{\text{local}}$ significantly reduces patch reconstruction errors, indicating improved latent–image spatial alignment.

tion achieves improved latent–image spatial alignment. In contrast, removing $\mathcal{L}_{\text{local}}$ disrupts the spatial alignment, indicating that the fine-tuned encoder entangles information across spatially distant latent tokens. Consequently, the latent–pixel mapping is no longer enforced to be spatially local, and applying CAA propagates information across unrelated regions, leading to degraded multi-view consistency and reduced overall performance, as observed in Tab. 1 of the main paper.

B. Implementation Details

In this section, we present implementation details for MATVAE (Sec. B.1) and MATLAT (Sec. B.2), along with the data preprocessing pipeline (Sec. B.3).

B.1. MATVAE

Architecture. Our MATVAE is initialized from the pre-trained VAE of Stable Diffusion 3.5–Medium. We freeze the original encoder \mathcal{E}_{pre} and decoder \mathcal{D}_{pre} , and introduce an offset encoder \mathcal{E}_{res} to adapt the latent space to 5-channel PBR inputs.

The offset encoder \mathcal{E}_{res} shares the same architecture as \mathcal{E}_{pre} except for the first convolution layer, which is modified to accept 5-channel inputs $[\mathbf{a}, \mathbf{r}, \mathbf{m}]$. All intermediate layers of \mathcal{E}_{res} are initialized from the corresponding weights of \mathcal{E}_{pre} , while the output layer is zero-initialized such that $\boldsymbol{\mu}_{\text{res}} = \mathbf{0}$ and $\boldsymbol{\sigma}_{\text{res}} = \mathbf{1}$ at initialization. The decoder \mathcal{D} extends the final convolution of \mathcal{D}_{pre} to output 5 channels; all other layers are copied from the pretrained decoder.

Training Configurations. We train MATVAE with the loss function in Eq. 8 of the main paper. We use the Adam

optimizer with learning rate 3×10^{-5} and batch size 8, training for 200k iterations on 8 NVIDIA RTX Pro6000 GPUs for 60 hours. The loss weights are set to $\lambda_{\text{local}} = 3$, $\lambda_{\text{KL}} = 10^{-6}$, $\lambda_{\text{disc}} = 0.02$, and $\lambda_{\text{reg}} = 3 \times 10^{-9}$. For locality regularization, we randomly crop a square region covering 5%–50% of the image area with probability 0.5.

B.2. Diffusion Model Fine-Tuning

Our diffusion model is built on STABLE DIFFUSION 3.5–MEDIUM with MMDiT [11] backbone. For each joint attention layer, we introduce a parallel correspondence-aware attention (CAA) branch that attends over geometrically corresponding pixels across views, using the precomputed 3D correspondences described in Sec. 3.2 of the main paper. The CAA branch uses the same base projection weights as the original joint attention layers, while introducing additional LoRA layers [20] with rank 32. The CAA output is added residually to the original attention output.

Additionally, to align the generated images with the input geometry, we follow previous works [2, 17, 22] and condition the diffusion model on rendered position and normal maps from the corresponding camera view. These geometric features are concatenated with the noisy latent to form the diffusion input.

Training Configurations. We optimize MATLAT using the Conditional Flow Matching [32] objective defined in Eq. 9 of the main paper. We use the Adam optimizer with learning rate 5×10^{-5} and batch size 4, training for 20k iterations on 8 NVIDIA RTX Pro6000 GPUs which takes about 24 hours.

Inference. At inference time, we generate multi-view images from $N = 6$ canonical views (front, back, left, right, top, and bottom) using the Euler sampler with 30 steps and a Classifier-Free Guidance [19] scale of 4.0. Given the generated PBR latent samples, we first decode them into 5-channel material images and then convert the multi-view PBR outputs into a final UV texture map following the pipeline of MVAdapter [22]: we upscale the images, unproject them into UV space using the given camera poses and mesh, and finally perform inpainting in UV space to fill occluded regions.

Baseline Implementations. For MeshGen [7] and MaterialMVP [17], which operate in an image-conditional setting, we use STABLE DIFFUSION 2-DEPTH to generate the reference images used as conditional inputs. All other baselines are evaluated using their official implementations with default configurations.

B.3. Data Processing

We curate 40,851 meshes with PBR textures from Objaverse-XL [8], holding out 128 meshes for evaluation. For each mesh, we render material images from 26 fixed camera views surrounding the object. We then render albedo, roughness, and metallic images, along with normal and position maps for conditioning, from each view. During diffusion training, we randomly sample 6 of these 26 views per iteration to construct the multi-view training batch. Additionally, for text conditioning, we use captions from BootStrap3D [42] when available; otherwise, we use captions from Cap3D [34].

During evaluation, we render the PBR-textured assets under environment lighting using 785 HDR environment maps from Poly Haven. For each image, we then randomly sample an environment map and apply the same rendering setup to both the generated and ground-truth images to ensure a fair comparison.

C. Additional Qualitative Results

In this section, we present a qualitative example for each of the ablation studies (Sec. C.1), baseline comparisons (Sec. C.2), and generated textures of MATLAT (Sec. C.3) as a representative reference. **Please refer to the project page for more results and video demonstrations:** <https://matlat-proj.github.io/>

C.1. Additional Qualitative Results of Ablation Studies

Fig. 9 extends the ablation study in Sec. 4.2 of the main paper with additional qualitative examples. We observe that Frozen VAE produces unrealistic material appearance, as evidenced by the overly shiny metallic shoe surface. Additionally, Res. Pred. + \mathcal{L}_{id} and Direct Pred. + \mathcal{L}_{reg} miss fine details such as *metal* buckles, whereas MATLAT generates PBR textures with correct and realistic material appearances.

C.2. Additional Qualitative Comparisons with Previous Methods

Fig. 10 presents qualitative comparisons against representative baselines, including models trained from scratch (MeshGen [7], TexGaussian [49]), SDS-based optimization methods (Paint-it [52], DreamMat [58], FlashTex [10]), and prior multi-view diffusion models (MaterialAnything [21], MaterialMVP [17]). Models trained from scratch often produce textures with suboptimal quality and exhibit weak alignment with the input text prompts. Additionally, SDS-based methods lack fine details and tend to generate textures with oversaturated colors. In contrast, our method MATLAT generates high-quality textures with realistic material properties.

C.3. Additional Qualitative Results

Extending the results in Fig. 6 of the main paper, we present additional PBR textures generated by our method MATLAT with diverse prompts, meshes, and environment maps in Fig. 11. Note that our method generates physically plausible material properties that are well aligned with both the object characteristics and the provided text prompt. These results demonstrate that our pipeline exhibits strong generalization across diverse object categories and material types.

Additional Qualitative Results of Ablation Studies



Figure 9. **Additional Qualitative Results of Ablation Studies.** Extended qualitative results of the ablation studies presented in Fig. 5 of the main paper: Frozen VAE, Res. Pred. + \mathcal{L}_{id} , Direct Pred. + \mathcal{L}_{reg} , and Res. Pred. + \mathcal{L}_{reg} (Ours). **Best viewed in video.**

Additional Qualitative Comparisons with Previous Methods



Figure 10. **Additional Qualitative Comparisons with Previous Methods.** Each column shows the shaded output rendered under identical lighting conditions. Our method produces high-quality, physically plausible materials with superior text-visual alignment and detail preservation. **Best viewed in video.**

Additional Qualitative Results of MatLat

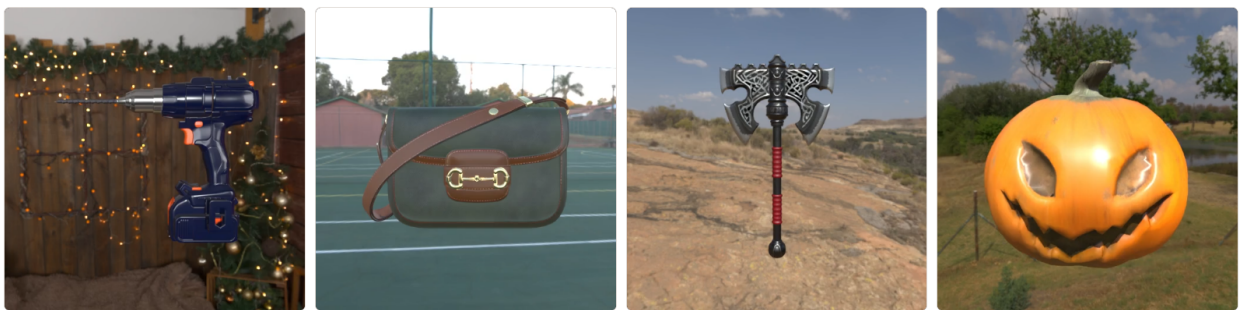


Figure 11. **Additional Qualitative Results of MATLAT.** Gallery of assets textured by our MATLAT for various text prompts and environment maps. **Best viewed in video.**